Journal of ELECTRONIC MATERIALS, Vol. 46, No. 11, 2017
DOI: 10.1007/s11664-017-5687-2
© 2017 The Minerals, Metals & Materials Society

Effects of Molybdenum Doping and Annealing on the Physical Properties of In_2O_3 Thin Films

NASREDDINE BEJI,[1,3,4] MEHDI SOULI,[1] MERIEM REGHIMA,[1] SONIA AZZAZA,[2] ALLEG SAFIA,[2] and NAJOUA KAMOUN-TURKI[1]

1.—LR99ES13 Laboratoire de Physique de la Matière Condensée (LPMC), Département de Physique, Faculté des Sciences de Tunis, Université Tunis El Manar, 2092 Tunis, Tunisie, Tunisia. 2.—Laboratoire de Magnétisme et Spectroscopie des Solides (LM2S), Département de Physique, Faculté des Sciences, Université Badji Mokhtar, B.P. 12, 23000 Annaba, Algeria. 3.—e-mail: beji.nasreddine@yahoo.fr. 4.—e-mail: beji.nasreddine@gmail.com

Molybdenum-doped In_2O_3 thin films with different atomic ratios of $y = \frac{[Mo^{6+}]}{[In^{3+}]}$ = 0 at.%, 1 at.%, 3 at.%, 5 at.%, and 7 at.% have been prepared by spray pyrolysis. X-ray diffraction (XRD) analysis showed that the Mo-doped In_2O_3 thin films crystallized in cubic structure with (222) preferred orientation. The best crystallinity was obtained for molybdenum concentration of 3 at.%, with an increase in grain size up to 155 nm. MAUD software was applied to the x-ray diffraction patterns to determine the phases, average grain size (d), microstrain ($\langle \sigma^2 \rangle^{1/2}$) and lattice parameters. The optical transmission was close to 75%. Doped films displayed large bandgap energy on the order of 3.52 eV to 3.56 eV. Optical parameters such as refractive index (n), packing density (p), porosity, oscillator energy (E_0), and dispersive energy (E_d) were studied using the envelope method. The electrical resistivity (ρ) decreased from 650.20×10^{-3} Ω cm to 2.03×10^{-3} Ω cm for undoped and In_2O_3:Mo(3 at.%) thin film, respectively. Heat treatment of In_2O_3:Mo(3 at.%) thin film under nitrogen atmosphere at 250°C for 2 h led to further decrease in the electrical resistivity to about 5.55×10^{-4} Ω cm. These results prove that annealed In_2O_3:Mo(3 at.%) thin film can be considered a key material for use in optoelectronic devices as a transparent electrode or an optical window for solar cells.

Key words: Thin films, spray pyrolysis technique, molybdenum doping, MAUD program, envelope method, annealing under nitrogen atmosphere

INTRODUCTION

In_2O_3 compound is a promising transparent conductive oxide (TCO) material due to its low resistivity and high transmission.[1] It can be used in many applications, e.g., in photovoltaic devices,[2] thin-film transistors,[3] light-emitting diodes,[4] and gas sensors.[5] Thanks to its simplicity, safety, low cost, and production of large-area films, spray pyrolysis appears to be one of the most efficient techniques for growth of such material. In this study, molybdenum-doped In_2O_3 thin films with atomic doping concentration $y = \left(\frac{[Mo^{6+}]}{[In^{3+}]}\right)_{sol}$ of 0 at.%, 1 at.%, 3 at.%, 5 at.%, and 7 at.% were obtained using the spray pyrolysis technique and their physical properties studied. Prathap et al. reported that the ionic radius of molybdenum is similar to that of indium (62 pm for Mo^{6+} versus 81 pm for In^{3+}), which facilitates incorporation of Mo^{6+} in the crystal lattice of In_2O_3.[6] This study highlights the effects of the molybdenum doping concentration and annealing on the physical

(Received January 24, 2016; accepted July 13, 2017; published online July 31, 2017)

properties of sprayed In_2O_3 thin films. Detailed structural analysis was carried out using MAUD software based on the Rietveld method to determine various structural and microstructural parameters such as the phase amounts, average grain size (d), microstrain ($\langle \sigma^2 \rangle^{1/2}$), and lattice parameters.[7] Moreover, the optical properties were extensively investigated using the envelope method[8] based on transmission and reflection spectra to investigate optical parameters such as the refractive index (n), packing density (p), porosity, oscillator energy (E_0), and dispersive energy (E_d). Films optimized using the doping process were annealed at different conditions to further enhance the physical and especially electrical properties of sprayed molybdenum-doped In_2O_3 layers. Several studies have investigated improvement of the physical properties of In_2O_3:Mo, but to the best of our knowledge, MAUD software, the envelope method, and annealing have never been applied to study sprayed Mo-doped In_2O_3 thin films.

The produced films were characterized by x-ray diffraction (XRD) analysis, atomic force microscopy (AFM), spectrophotometry, and Hall-effect measurements.

EXPERIMENTAL PROCEDURES

Molybdenum-doped indium oxide thin films were grown by the pulverization technique in liquid phase (spray) with indium chloride ($InCl_3$) and molybdenum chloride ($MoCl_5$) powders as precursors and double-distilled water as solvent. In_2O_3:Mo thin films were formed on glass substrates at 500°C with compressed air as carrier gas. The solution flow rate was fixed at 2.5 ml min^{-1}. The experimental setup was described previously.[9] The atomic concentration of molybdenum in the solution (y) was varied to $y = \left(\frac{[Mo^{6+}]}{[In^{3+}]}\right)$ = 0 at.%, 1 at.%, 3 at.%, 5 at.%, and 7 at.%. The structure of the layers was studied by x-ray diffraction (XRD) analysis using an automated Bruker D8 advance x-ray diffractometer with Cu K_α radiation in the 2θ range from 10° to 70° at wavelength, accelerating voltage, and current of 1.5418 Å, 40 kV, and 20 mA, respectively. The morphology of the surface of each film was studied by atomic force microscopy (AFM, standard Veeco Dimension 3100) in tapping mode. Optical transmission and reflection measurements were carried out using a Perkin-Elmer Lambda 950 spectrophotometer in the wavelength range of 250 nm to 2500 nm at room temperature with air as reference. Resistivity (ρ), carrier concentration (N_v), and mobility were measured using the Hall effect in van der Pauw configuration. Annealing was performed using a Jet First Processor™. X-ray diffraction patterns were refined using MAUD program based on Rietveld analysis.[7]

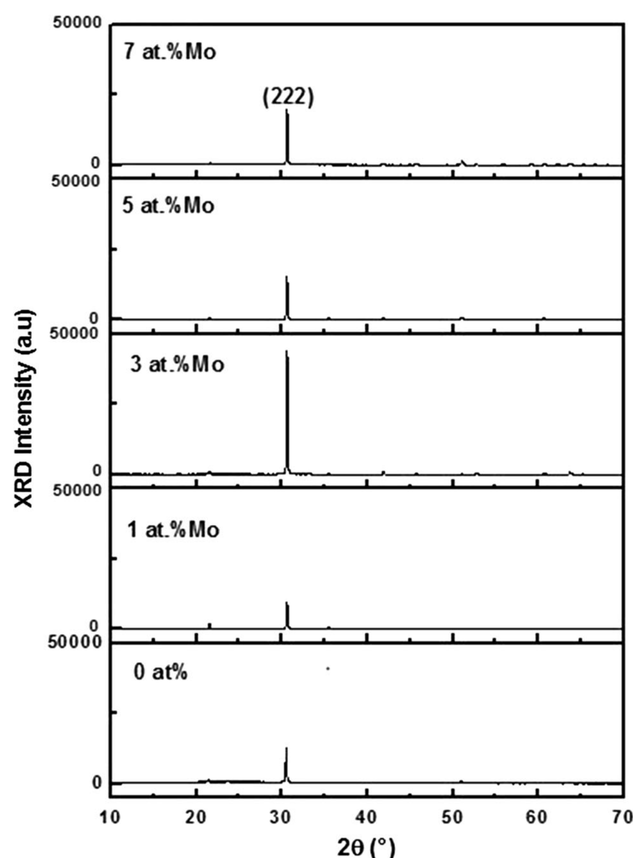

Fig. 1. XRD patterns of Mo-doped In_2O_3 thin films with different doping concentrations $y = \left(\frac{[Mo^{6+}]}{[In^{3+}]}\right)_{sol}$ = 0 at.%, 1 at.%, 3 at.%, 5 at.%, and 7 at.%.

DOPING EFFECT

Structural Properties

XRD Analysis

X-ray diffraction patterns of molybdenum-doped indium oxide thin films with different concentrations y ($y = \left(\frac{[Mo^{6+}]}{[In^{3+}]}\right)$ = 0 at.%, 1 at.%, 3 at.%, 5 at.%, and 7 at.%) are shown in Fig. 1. Note that the doped In_2O_3 films crystallized in body-centered cubic (bcc) structure, as is the case for undoped layers according to Joint Committee on Powder Diffraction Standards (JCPDS) card no. 06-0416. The peaks were very narrow, indicating good crystallinity. A main diffraction peak was located at approximately 2θ = 30.50°, corresponding to (222) plane. A sharp increase in the strongest orientation (222) was observed for y = 3 at.% compared with undoped film. This result corresponds to enhanced crystal quality due to the doping process. Indeed, up to 3 at.% Mo^{6+} ions may substitute for In^{3+} ions in the crystal lattice. Similar behavior was observed by Kaleemulla et al.[10] for Mo-doped In_2O_3 films obtained using an activated reactive evaporation method. Beyond 3 at.%, a gradual decrease in (222)

Table I. Structural parameters of Mo-doped In_2O_3 thin films with different concentrations y $\left(y = \frac{[Mo^{6+}]}{[In^{3+}]}\right)_{sol}$ = 0 at.%, 1 at.%, 3 at.%, 5 at.%, and 7 at.%

Structural parameters from XRD curves					Structural parameters from MAUD software						
								Lattice parameters (Å) (±0.0002)			
y (at.%)	2θ (°)	FWHM (°)	d (nm)	t (nm)	Phase	d (nm) (±1.5)	$\langle\sigma^2\rangle^{1/2}$ (%) (±0.01)	a	b	c	Phase amount (%) (±1)
0	30.49	0.1710	71	750	In_2O_3	–	0.0208	10.1280	–	–	100
1	30.61	0.1550	90	904	In_2O_3	105	0.0214	10.1247	–	–	100
3	30.61	0.1359	155	949	In_2O_3	153	0.0179	10.1250	–	–	96.31
					MoO_3	99.98	0.102	3.93822	13.9313	3.66085	3.69
5	30.60	0.1440	115	1096	In_2O_3	101	0.0254	10.1242	–	–	93.95
					MoO_3	99.99	0.143	3.94026	13.9459	3.66258	6.05
7	30.62	0.1385	138	1106	In_2O_3	103	0.0221	10.1241	–	–	91.75
					MoO_3	97.67	0.135	3.94025	13.9459	3.66257	8.25

FWHM, full-width at half-maximum.

peak intensity was observed compared with that for y = 3 at.%. This deterioration of the crystallinity can be attributed to stress formation caused by the difference in ion size between indium and molybdenum.[9] The variation of the diffraction angle 2θ for (222) plane as a function of the atomic concentration y is presented in Table I. A slight increase in the diffraction angle for the doped films compared with the undoped film was noted. According to Bragg's law ($2D\sin\theta = n\lambda$), this increase in the diffraction angle θ corresponds to a decrease in the interplanar distance D, i.e., contraction of the crystal lattice.

The grain size (d) of the films with different doping concentration y was calculated using the Scherrer formula applied to the (222) preferred orientation[11]:

$$d = \frac{0.94\lambda}{\sqrt{\beta^2 - \beta_0^2}\cos\theta},$$

where λ is the x-ray wavelength of Cu K_α radiation (λ = 1.5418 Å), $\beta_0 = 0.125°$ is the width of the corresponding peak due to instrumental broadening, β is the experimental full-width at half-maximum (FWHM) of the diffraction peak with preferential orientation measured in radians, and θ is Bragg's angle.

The average grain size (d) deduced from the Scherrer formula for different molybdenum concentrations y is summarized in Table I, showing that d tended to be larger after the doping process. In fact, d lay in the range of 101 nm to 155 nm for the doped layers and around 71 nm for undoped film. In_2O_3:Mo(3 at.%) thin film exhibited a maximum value of grain size equal to 155 nm. Therefore, the elaborated layer with doping ratio of 3 at.% exhibited the best crystallinity.

Rietveld Analysis

X-ray diffraction (XRD) patterns of molybdenum-doped In_2O_3 thin films were refined using the MAUD program based on the Rietveld method. The results, including the lattice parameters, grain size, microstrain ($\langle\sigma^2\rangle^{1/2}$), and phase amounts, are summarized in Table I. Presence of two phases was noted, viz. In_2O_3 and MoO_3, as shown in Table I. For $y \geq 3$ at.%, MoO_3 secondary phase was detected at low amounts compared with In_2O_3 phase. This phase crystallized in orthorhombic structure. It is clear from Table I that the content of molybdenum oxide phase increased with the doping concentration y, reaching a maximum of 8.25% for 7 at.%. The absence of undesirable phases for 1 at.% doping can be explained as follows: At this doping level, the small amount of molybdenum element added can be fully incorporated into the In_2O_3 crystal lattice. On the other hand, the lattice parameter a corresponding to the body-centered cubic In_2O_3 structure decreased after doping. Hence, contraction of the crystal lattice compared with undoped film was observed, in good agreement with the investigation based on Bragg's law. This result can be attributed to the fact that the ionic radius of Mo^{6+} (62 pm) is smaller than that of In^{3+} (81 pm). The grain size (d) as a function of doping concentration y was also calculated using the MAUD program. d showed a maximum value on the order of 153 nm for y = 3 at.%, revealing the improvement of crystallinity. The deduced grain size values are well consistent with those calculated

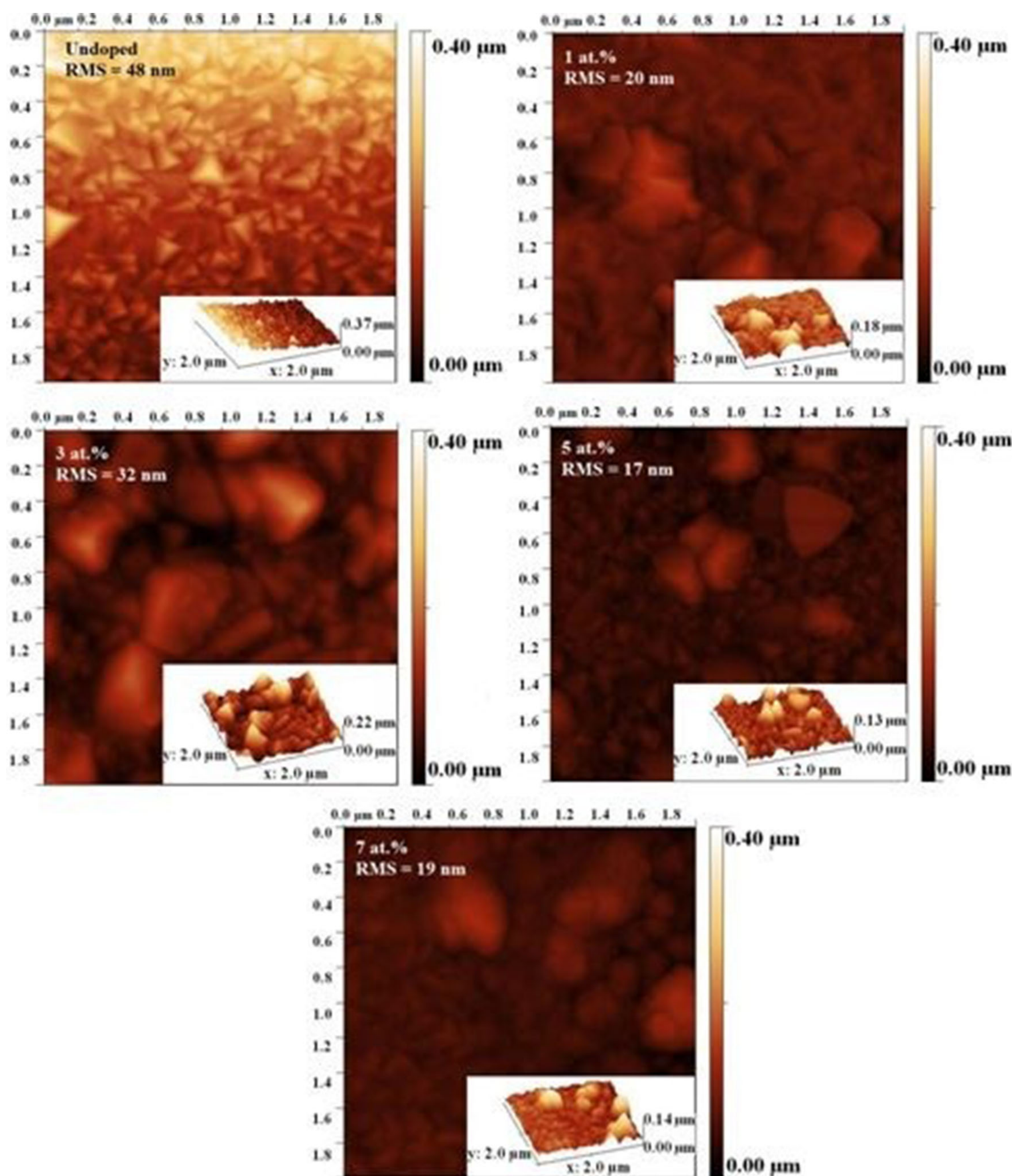

Fig. 2. AFM images (2D and 3D) and RMS roughness values of undoped and Mo-doped In_2O_3 thin films with different concentrations y $\left(y = \frac{[Mo^{6+}]}{[In^{3+}]}\right)_{sol}$ = 0 at.%, 1 at.%, 3 at.%, 5 at.%, and 7 at.%.

using the Scherrer formula. The microstrain $\langle\sigma^2\rangle^{1/2}$ increased after doping except for y = 3 at.%. At this doping level, the microstrain reached a minimum value of 0.0179% corresponding to the best crystallinity, which is also in accordance with the x-ray diffraction (XRD) analysis.

Morphological Properties

Figure 2 displays atomic force microscopy (AFM) images of Mo-doped In_2O_3 thin films. For doped films, the AFM images reveal the appearance of large agglomerates of crystallites over a dense texture. An increase in crystallite size after doping is observed. This result is in good agreement with the structural analysis, based on which it was found that the grain size tended to be larger for the doped films. It is also worth noting that the density and size of the agglomerated grains depended on the molybdenum doping ratio. The root-mean-square (RMS) roughness values for different doping concentrations y are shown in Fig. 2. A remarkable

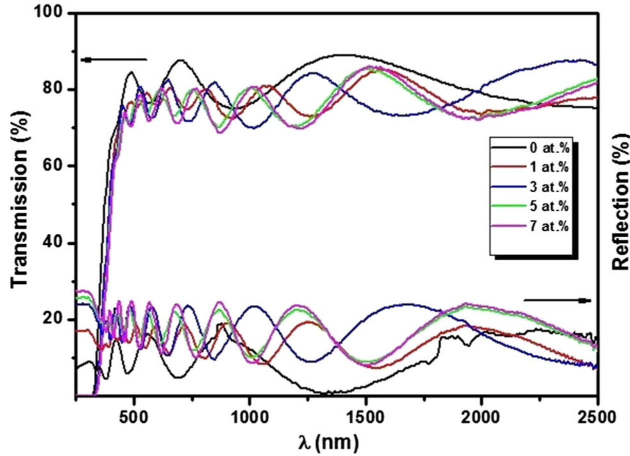

Fig. 3. Transmission and reflection spectra of Mo-doped In_2O_3 thin films with different doping concentrations $y\left(y=\frac{[Mo^{6+}]}{[In^{3+}]}\right)_{sol}$ = 0 at.%, 1 at.%, 3 at.%, 5 at.%, and 7 at.%.

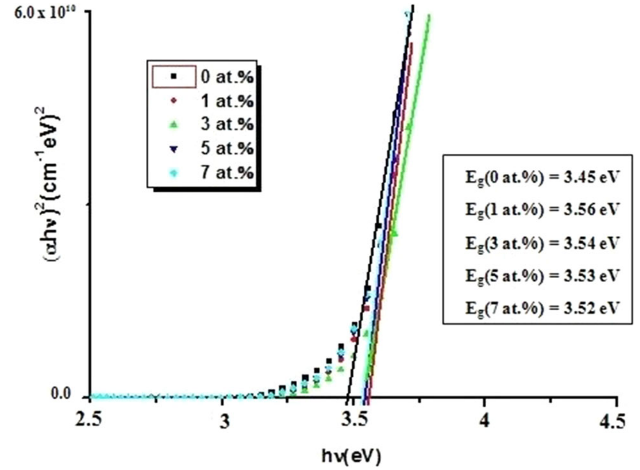

Fig. 4. Variation of $(\alpha h\nu)^2$ versus $(h\nu)$ for Mo-doped In_2O_3 thin films with different doping concentrations $y\left(y=\frac{[Mo^{6+}]}{[In^{3+}]}\right)_{sol}$ = 0 at.%, 1 at.%, 3 at.%, 5 at.%, and 7 at.%.

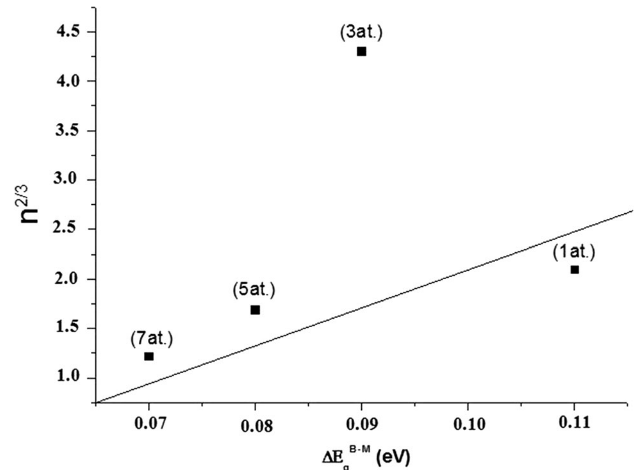

Fig. 5. $n^{\frac{2}{3}}$ versus Burstein–Moss shift (ΔE_g^{B-M}).

decrease in the RMS value after doping was noted. In fact, the RMS value was on the order of 17 nm to 32 nm for the doped layers but around 48 nm for the undoped layer. Therefore, doping with molybdenum enhanced the surface uniformity of the elaborated layers.

Optical Properties

The transmission and reflection spectra of molybdenum-doped In_2O_3 thin films are displayed in Fig. 3. It is shown that the molybdenum affected the optical properties of the elaborated layers. The doped films presented multiplied oscillation compared with the undoped layer, corresponding to enhanced thickness uniformity and film homogeneity after doping. Although the transmission (T) declined slightly after doping, it remained high at about 75% in the visible as well as near-infrared region. Such a decrease of the transmission may be due to increased light absorption due to increased film thickness after doping. Therefore, a decline in the film transparency was observed. In fact, the film thickness (t) was about 750 nm for undoped film. However, t ranged from 904 nm to 1106 nm for the doped layers, corresponding to a lower transmission level than for the undoped film. Similar results have been obtained for other doped In_2O_3 films, such as In_2O_3:Zn,[12] In_2O_3:Mo,[13] and In_2O_3:Li.[14] The optical bandgap of the elaborated thin films was calculated as a function of the molybdenum doping concentration y using the Tauc equation[15]:

$$(\alpha h\nu) = A\left(h\nu - E_g\right)^n, \tag{2}$$

where $(h\nu)$ is the photon energy, h is Planck's constant, n is equal to ½ for a direct bandgap, A is a constant, and α is the absorption coefficient.

To determine the energy bandgap value, one must find the linear relation between $(\alpha h\nu)^{1/n}$ and $(h\nu)$ according to the Tauc equation. The bandgap energy (E_g) was obtained by extrapolating the linear part of the Tauc curves $(\alpha h\nu)^2$ to the intercept with the energy axis $(h\nu)$ (Fig. 4). Only for n = ½ did we observe a linear relation between $(\alpha h\nu)^2$ and $(h\nu)$. This observation confirms that our elaborated films exhibited a transition of direct type.[12,16]

The bandgap energy (E_g) of the doped films ranged between 3.52 eV and 3.56 eV. However, E_g was 3.45 eV for undoped film. Such an increase of the optical bandgap can be explained using the Burstein–Moss effect as follows[17]:

$$E_g = E_{g0} + \Delta E_g^{B-M}, \tag{3}$$

where E_{g0} and ΔE_g^{B-M} are the intrinsic band energy and Burstein–Moss shift, respectively, due to the filling of low levels in the conduction band.

Table II. Optical parameters and Hall-effect results of undoped and Mo-doped In_2O_3 thin films for molybdenum doping concentration $y \left(y = \frac{[Mo^{6+}]}{[In^{3+}]}\right)_{sol}$ = 0 at.%, 1 at.%, 3 at.%, 5 at.%, and 7 at.%

y (at.%)	E_0 (eV)	E_d (eV)	S_0 (10^{-5} nm^{-2})	λ_0 (nm)	Resistivity, ρ (Ω cm)	Hall mobility, μ (cm^2/V-s)	Volume carrier concentration, $N_v \times 10^{19}$ (cm^{-3})
0	5.05	15.02	4.93	245.54	650.20×10^{-3}	1.17	0.80
1	6.87	14.73	6.58	180.50	19.10×10^{-3}	10.79	3.03
3	6.92	15.70	7.06	179.20	2.03×10^{-3}	34.67	8.85
5	7.16	15.21	7.08	173.20	195×10^{-3}	14.62	2.19
7	7.00	15.30	6.97	177.14	210×10^{-3}	22.11	1.35

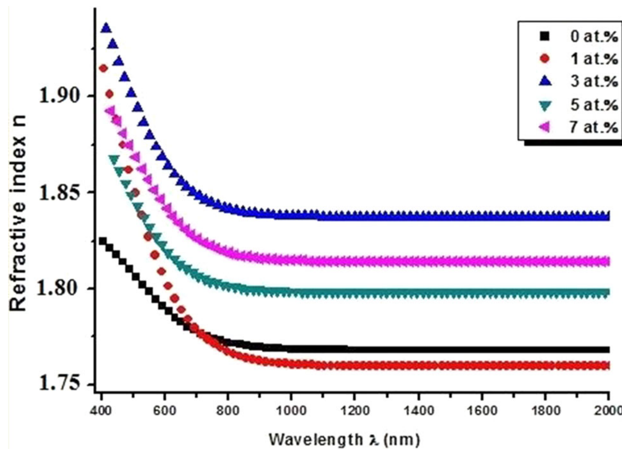

Fig. 6. Refractive index (n) of Mo-doped In_2O_3 thin films with different doping concentrations $y \left(y = \frac{[Mo^{6+}]}{[In^{3+}]}\right)_{sol}$ = 0 at.%, 1 at.%, 3 at.%, 5 at.%, and 7 at.%.

The Burstein–Moss shift can be expressed as[17]

$$\Delta E_g^{B-M} = \frac{h^2}{8m_{vc}^* \pi^2} \left(3n\pi^2\right)^{2/3}, \quad (4)$$

where n and m_{vc}^* are the carrier concentration and reduced effective mass, respectively.

The graph of ΔE_g^{B-M} versus $n^{\frac{2}{3}}$ is presented in Fig. 5. It is shown that the B–M shift is approximately proportional to $n^{2/3}$ for all the doping concentrations except 3 at.%.

Using the same beamline, Pramod et al.[14] found an increase in the bandgap energy after doping In_2O_3 with lithium. They explained that the increase in free carrier concentration after doping (Table II) can be ascribed to the widening of the bandgap, which is in good accordance with our results. Moreover, the secondary phase molybdenum oxide (MoO_3) exhibits a large bandgap in the range of 3.20 eV to 3.72 eV.[18] Such effects may contribute to the broadening of the bandgap energy (E_g).

Based on the envelope method, the refractive index n was calculated for different molybdenum doping concentrations y using the following expressions[8]:

$$n(\lambda) = \left[N + \left(N^2 - n_0^2 n_{sub}^2\right)^{1/2}\right]^{1/2} \quad (5)$$

and $N = 2n_0 n_{sub}\left[\frac{(T_{max}-T_{min})}{(T_{max}T_{min})}\right] + \left(\frac{n_0^2+n_{sub}^2}{2}\right)$, where n_0 is the refractive index of air and n_{sub} is the refractive index of the glass substrate (1.52).

The obtained results are given in Fig. 6. The refractive index n is presented as a function of wavelength in the visible and near-infrared region. The refractive index increased after doping in the visible range. These n values are in accordance with the transmission reduction for the doped layers. The highest refractive index was found for doping ratio of 3 at.% (Fig. 6).

The refractive index (n) showed Cauchy behavior according to the equation[19]

$$n(\lambda) = A + \frac{B}{\lambda^2}, \quad (6)$$

where A and B are constants.

Indeed, the refractive index (n) was approximately constant at higher wavelengths. This result proves the Cauchy behavior of the refractive index.

The thickness (t) of the molybdenum-doped In_2O_3 thin films was calculated from the transmission–reflection spectra. Using this approach, t is determined from two maxima or minima using the following formula[20]:

$$t = \frac{M\lambda_1\lambda_2}{2(\lambda_1 n_2 - \lambda_2 n_1)}, \quad (7)$$

where M is the number of oscillations between two extrema (M = 1 between two consecutive maxima or minima). n_1 and n_2 are the refractive indexes of two adjacent maxima or minima at λ_1 and λ_2.

The calculated thicknesses (t) are presented in Table I. As shown, t increased after doping, leading to a reduction of transmission as proved in Fig. 4. Ajili et al.[9] obtained a similar result for Sn-doped ZnO thin layers elaborated by spraying.

Based on the refractive index values, the packing density (p) was calculated for different molybdenum

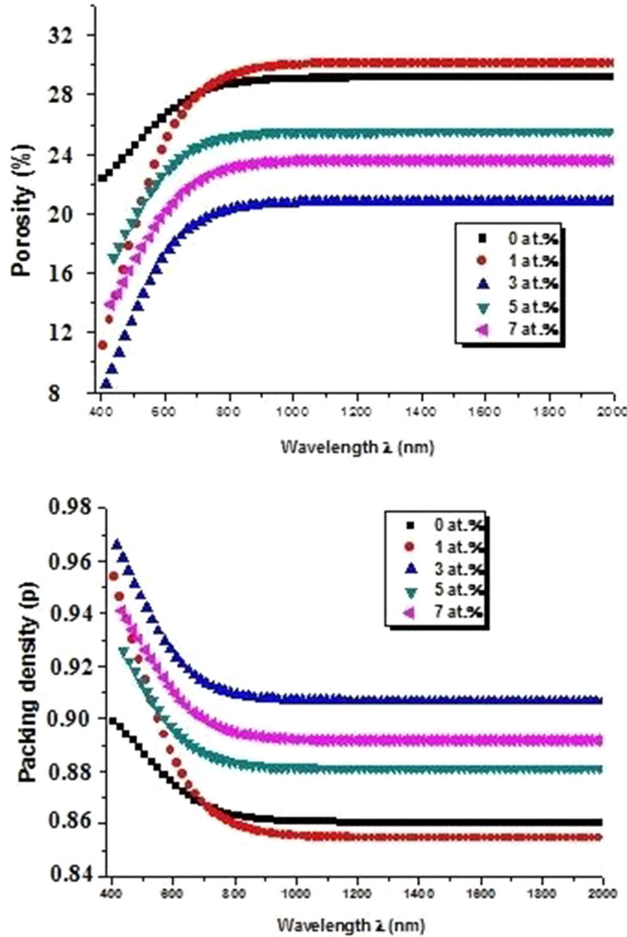

Fig. 7. Packing density (p) and porosity of Mo-doped In_2O_3 thin films with different doping concentrations y $\left(y = \frac{[Mo^{6+}]}{[In^{3+}]}\right)_{sol}$ = 0 at.%, 1 at.%, 3 at.%, 5 at.%, and 7 at.%.

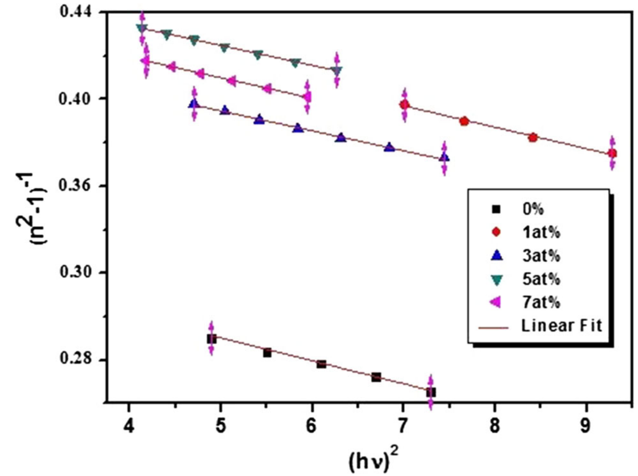

Fig. 8. Variation of $(n^2 - 1)^{-1}$ as function of $(h\nu)^2$ of Mo-doped In_2O_3 thin films with different concentrations y $\left(y = \frac{[Mo^{6+}]}{[In^{3+}]}\right)_{sol}$ = 0 at.%, 1 at.%, 3 at.%, 5 at.%, and 7 at.%.

concentrations y using the Bragg and Pippard model,[21] as modified by Harris et al.,[22] according to the following equation:

$$n^2 = \frac{(1-p)n_v^4 + (1+p)n_v^2 n_s^2}{(1+p)n_v^2 + (1-p)n_s^2}, \quad (8)$$

where n_v is the void refractive index (1 for air) and n_s is the bulk value of the refractive index.

The porosity of all the films was also investigated based on the refractive index results according to[23]

$$\text{Porosity} = \left(1 - \frac{n^2 - 1}{n_d^2 + 1}\right) \times 100\%, \quad (9)$$

where n_d is the refractive index of pore-free In_2O_3 (i.e., 2[24]) and n is the refractive index of the porous In_2O_3 thin films.

The results are presented in Fig. 7. As observed, the packing density (p) lay in the range from 0.86 to 0.97. The obtained packing density values are in the same range as those found by Senthilkumar et al.[23] for indium tin oxide (ITO) films. Nevertheless, p took its highest values for the doped layers in the visible range compared with the undoped layer, in support of the refractive index studies. Note that p was maximum for 3 at.%, which corresponds to the best crystallinity. As seen in Fig. 7, the porosity decreased in the visible range for the doped films. The thin film grown with 3 at.% was the least porous, leading to greater homogeneity.

The oscillator energy (E_0) and dispersion energy (E_d) were determined using the Wemple model[25]:

$$n^2 - 1 = \frac{E_d E_0}{E_0^2 - (h\nu)^2}, \quad (10)$$

where n is the refractive index.

Figure 8 shows the linear variation of $(n^2 - 1)^{-1}$ versus $(h\nu)^2$ for the molybdenum-doped indium oxide thin films. E_0 and E_d were determined from the slope $(E_d E_0)^{-1}$ and the intercept at the origin (E_0/E_d) for each doping ratio.

The average strength S_0 and wavelength λ_0 of the oscillator were deduced from the Wemple equation as follows:

$$\lambda_0 = \frac{hc}{E_0}, \quad (11)$$

$$S_0 = \frac{E_0 E_d}{(hc)^2}. \quad (12)$$

The deduced Wemple results are presented in Table II, showing that $E_0 = 2 \times E_g$ for the molybdenum-doped films. However, $E_0 = 1.5 \times E_g$ for the undoped film. The oscillator energy E_0 increased after doping, in agreement with the expand band-gap energy E_g for the doped films. Similar results were found in our previous studies on iron-doped In_2O_3 thin films[26] and zinc-doped In_2O_3 thin films.[27]

Electrical Properties

The electrical properties of the molybdenum-doped In_2O_3 thin films as derived from Hall-effect measurements are presented in Table II. The resistivity decreased drastically from $650.20 \times 10^{-3}\ \Omega$ cm to $2.03 \times 10^{-3}\ \Omega$ cm for undoped and In_2O_3:Mo(3 at.%) thin films, respectively. This decrease of resistivity can be attributed to the difference between the electronic valences. In fact, introduction of Mo^{6+} ions into the indium oxide matrix leads to release of three electrons in the In_2O_3 lattice, which induces the increase of conductivity.[28] This reduction may also be attributed to the increase in mobility (μ) and carrier concentration (N_v) by an order of magnitude. Indeed, for y = 3 at.%, a remarkable increase of the Hall mobility from 1.17 cm^2/V-s to 34.67 cm^2/V-s was observed compared with the undoped film. Similarly, the volume carrier concentration (N_v) increased from 0.80×10^{19} cm^{-3} to 8.85×10^{19} cm^{-3}. Such an increase of N_v may be related to the improvement of crystallinity. Consequently, this contributes to the reduction of trap sites at grain boundaries.[29] From 5 at.%, a gradual increase in resistivity followed by a decrease in mobility was observed. In fact, the resistivity reached 210 x $10^{-3}\ \Omega$ cm for 7 at.%.

ANNEALING EFFECT

The study on the physical properties of the molybdenum-doped In_2O_3 thin films proved that the film doped at y = 3 at.% exhibited the best structural and optoelectronic properties. Based on this result, heat treatment was performed on the optimized In_2O_3:Mo(3 at.%) under nitrogen gas at T_a = 250°C and 450°C during 1 h to 2 h, to further enhance the structural, optical, and electrical properties.

Structural Properties

XRD patterns of In_2O_3:Mo(3 at.%) thin films annealed using different conditions are presented in Fig. 9. All peaks of the heated layers were very narrow, indicating good crystallinity. The diffraction peaks of the annealed films matched well with those of the body-centered cubic structure, as was the case for the as-deposited films. A small decrease in peak intensity for the preferred orientation along (222) plane was observed for the sample annealed at 250°C for 1 h. On increasing the annealing time to 2 h at 250°C, a gradual increase of peak intensity was noted. This increase was also observed at 450°C for 1 h. In fact, for this annealing condition, the intensity of the strongest peak was close to that for the as-deposited state. This can be explained as a result of rearrangement of atoms in the crystal lattice along (222) plane. Therefore, it can be deduced that heat treatment did not affect the preferential direction, but did assist with grain growth. Prolongation of the annealing time to 2 h at the higher annealing temperature (450°C) may contribute to the creation of atomic disorder, which could contribute to orientation of grains into different plane orientations, causing crystallinity degradation. Zhu et al.[30] found similar XRD behavior in terms of intensity for ZnO layers annealed in air at 150°C, 300°C, and 450°C. On the other hand, after annealing treatment of Mo-doped In_2O_3 thin films at 400°C, 500°C, and 600°C under vacuum, Shin et al.[4] found enhanced crystallinity and that the (222) texture was retained.

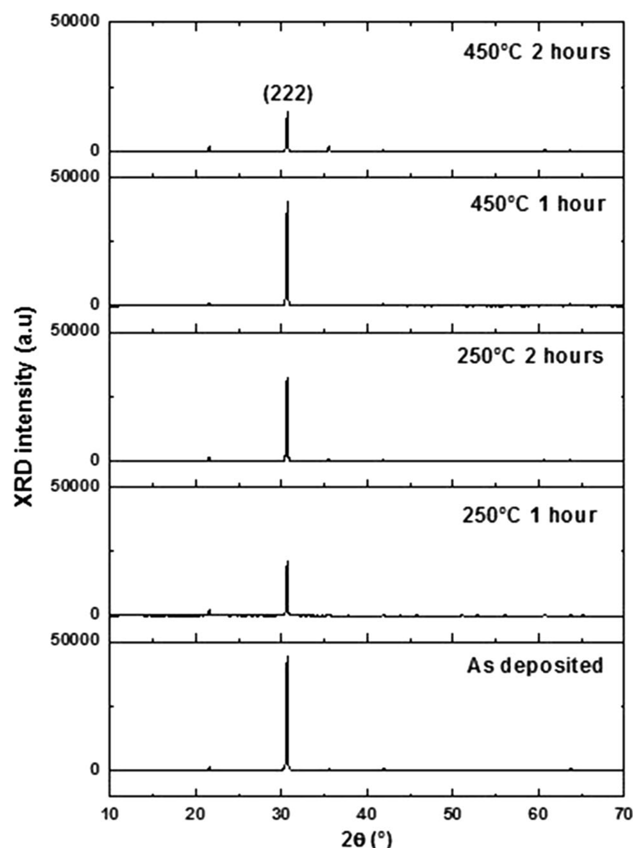

Fig. 9. XRD patterns of In_2O_3:Mo(3 at.%) after annealing at different conditions.

The grain size of the annealed films was calculated using the Scherrer formula, and the results are presented in Table III. A decrease of grain size after heat treatment was noted. In fact, the heated films exhibited grain size (d) in the range of 119 nm to 139 nm. However, d was on the order of 155 nm in the as-deposited state. This last finding can be attributed to the fact that crystallinity was deteriorated by heating. A similar result was obtained by Kim et al. after annealing ZnO:Al in N_2 gas.[31] In fact, they found a degradation of the film's crystallinity after heating followed by a decrease in grain size.

Table III. Structural parameters, optical bandgap energy, and Hall-effect measurements of In_2O_3:Mo(3 at.%) thin films annealed at different conditions

Annealing condition	Position of (222) peak, 2θ (°)	FWHM (°)	Grain size, d (nm)	RMS (nm)	E_g (eV)	Resistivity, ρ (Ω cm)	Hall mobility, μ (cm^2/V-s)	Volume carrier concentration, N_v (cm^{-3})
As deposited	30.61	0.1359	155	20	3.54	2.03×10^{-3}	34.67	8.85×10^{19}
250°C, 1 h	30.62	0.1392	134	46	3.54	9.58×10^{-4}	42.90	1.52×10^{20}
250°C, 2 h	30.62	0.1390	135	52	3.59	5.55×10^{-4}	42.69	1.63×10^{20}
450°C, 1 h	30.64	0.1383	139	12	3.65	4.34×10^{-3}	20.66	6.96×10^{19}
450°C, 2 h	30.64	0.1427	119	27	3.56	1.41×10^{-3}	22.38	1.98×10^{20}

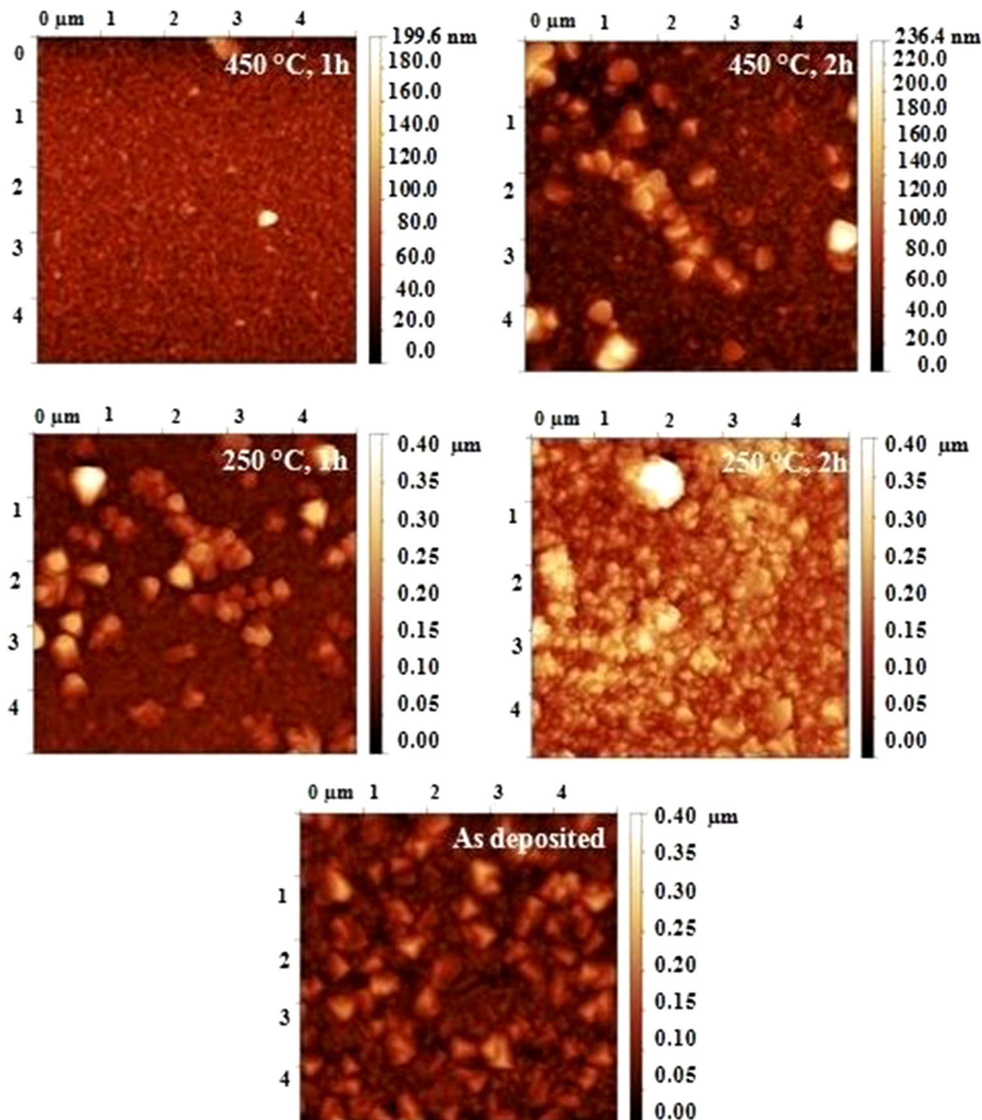

Fig. 10. AFM surface topography of In_2O_3:Mo(3 at.%) thin films annealed at different conditions.

Morphological Properties

AFM images of In_2O_3:Mo(3 at.%) thin films annealed at different conditions are presented in Fig. 10. The annealing temperature and time significantly affected the surface topography. Indeed, a modification of the grain form and size was noted for the annealed films, since they exhibited different textures. As seen, the grain sizes

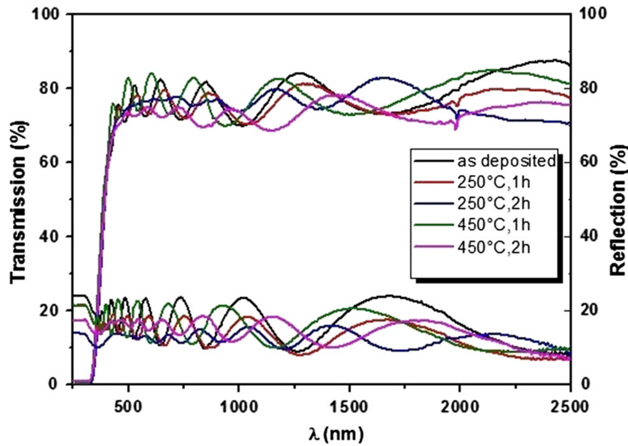

Fig. 11. Transmission and reflection spectra of In_2O_3:Mo(3 at.%) annealed at different conditions.

tended to be smaller for the annealed films, in good accordance with the calculations based on the Scherrer formula.

The RMS roughness values were extracted from the AFM images, and the results are presented in Table III. The highest RMS value was obtained for the films annealed at 250°C for 2 h. An increase in the RMS roughness values with increasing annealing time was revealed. Indeed, the RMS roughness reached 52 nm and 27.5 nm instead of 46 nm and 12 nm for the annealed films at 2 h and 1 h, respectively. Meanwhile, with increasing annealing temperature, the films looked smoother and more uniform. Hence, the RMS value decreased significantly; For example, for the films annealed for 1 h, the RMS value decreased from 46 nm to 12 nm for 250°C and 450°C, respectively.

Optical Properties

The transmission and reflection spectra of the annealed Mo-doped films with $y = 3$ at.% are shown in Fig. 11. Note the presence of interference fringes for all films, confirming the homogeneity and surface uniformity of the films after heat treatment. The average transmission of the annealed films was about 75%, reaching a higher value for the films annealed at 450°C for 1 h. This last result may be due to low carrier concentration, as mentioned in "Electrical Properties" section. For the films annealed at 250°C for 2 h, attenuation of the interference fringes in the visible region was observed. This may be due to high surface roughness, as observed from the AFM images, leading to enhanced photon scattering due to crystal defects.

The bandgap (E_g) was estimated using the Tauc equation, and the obtained results are given in Table III. An increase in the optical bandgap energy (E_g) was found for the annealed films compared with the as-deposited state. However, at given annealing temperature, E_g practically did not change as a function of annealing time.

Electrical Properties

The electrical properties of the heated layers were determined using Hall-effect measurements. The results are presented in Table III. The resistivity (ρ) of the films annealed at 250°C for 1 h decreased compared with the as-deposited state, from $2.03 \times 10^{-3}\ \Omega$ cm to $9.58 \times 10^{-4}\ \Omega$ cm. Prolonging the annealing time at the same temperature of 250°C led to a further decrease of ρ, reaching a minimum of about $5.55 \times 10^{-4}\ \Omega$ cm. At this annealing condition, high mobility on the order of 42.69 cm^2/V-s was recorded. This result can be ascribed to lower scattering frequency, as proven by the following equation[32]:

$$\mu = \frac{1}{ne\rho} = \frac{e}{fm^*}, \tag{13}$$

where n is the carrier concentration, e is the electron charge, ρ is the resistivity, f is the free electron scattering frequency, and m^* is the effective electron mass.

Note that the free carrier concentration (N_v) increased significantly from 8.85×10^{19} cm^{-3} to 1.63×10^{20} cm^{-3} for the as-deposited films and those heated at 250°C for 2 h, respectively. On increasing the annealing temperature (T_a) to 450°C, the resistivity rose again, with a decrease of the mobility.

The mean free path of an electron can be calculated using the equation[4]

$$l = \left(3\pi^2\right)^{1/3} x \left(\frac{h}{2\pi e^2}\right) x \frac{1}{\rho} x \left(n^{-\frac{2}{3}}\right), \tag{14}$$

where l is the mean free path, h is Planck's constant, e is the electron charge, ρ is the resistivity, and n is the carrier concentration.

The calculated mean free path (l) of an electron in the In_2O_3:Mo(3 at.%) thin films annealed at different conditions is presented in Fig. 12. Note that the mean free path increased with increasing annealing duration, while it decreased with annealing temperature. The longest l was found to be on the order of 4.89 nm for films annealed at 250°C for 2 h, which presented the best electrical properties. The obtained values of mean free path are much shorter than the grain size measured according to XRD analysis. Shin et al.[4] found similar results for annealed In_2O_3:Mo(3 at.%) thin films grown by heterotarget sputtering. They reported that the effect of scattering at dislocations and grain boundaries may be neglected when the mean free path is smaller than the grain size, and concluded that scattering of conduction electrons mainly depended on ionized and neutral impurities.[4]

While most studies have tended to focus on ZnO and SnO_2 materials for use as TCOs in solar cells, we believe that the current study shows better results for In_2O_3 layers. In fact, Manoharan et al.[33] obtained high resistivity ($1.27 \times 10^3\ \Omega$ cm) compared with the

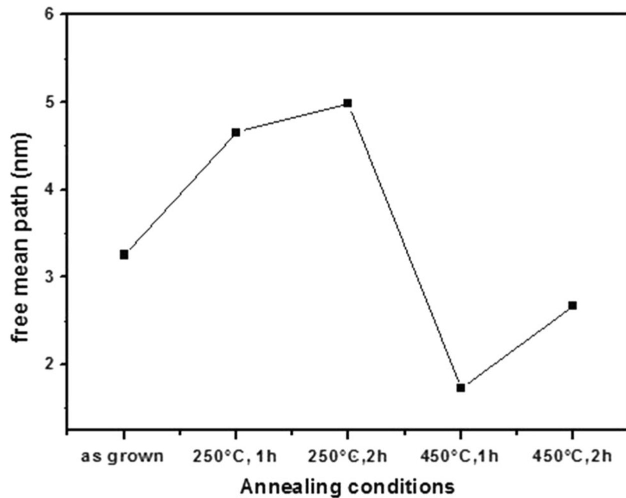

Fig. 12. Calculated mean free path (l) of electron for y = 0.3 at.% as function of annealing conditions.

result found herein (5.55×10^{-4} Ω cm). Moreover, those authors found low volume free carrier concentration (N_v) and Hall mobility (μ) of 7.25×10^{14} cm^{-3} and 6.40 cm^2/V-s, respectively, compared with 1.63×10^{20} cm^{-3} and 42.69 cm^2/V-s herein. On the other hand, Rahal et al.[34] elaborated tin oxide thin films, finding a drastic decrease in transmission reaching 44%, which is not encouraging for use as a good TCO. Moreover, they reported resistivity on the order of 9.19×10^{-3} Ω cm.

CONCLUSIONS

Molybdenum-doped indium oxide thin films were elaborated by spray pyrolysis. Doping was carried out during growth by adding different concentrations of Mo^{6+} ions to the sprayed solution. The physical properties of In_2O_3:Mo were improved after doping with molybdenum. X-ray diffraction (XRD) analysis revealed enhanced crystallinity for doping ratio of 3 at.%, with larger grain size of about 155 nm. The optical properties showed a small decrease in transmission after doping. The doped films exhibited high transmittance of around 75% in the visible and near-infrared regions, with the presence of interference fringes revealing their surface homogeneity. The calculated bandgap values ranged from 3.45 eV to 3.56 eV. The electrical resistivity decreased after doping from $\rho = 650.20 \times 10^{-3}$ Ω cm to 2.03×10^{-3} Ω cm for undoped and In_2O_3:Mo(3 at.%) thin films, respectively. The film doped at 3 at.% exhibited the best structural and optoelectronic properties. Based on this result, heat treatment was applied to further enhance the physical properties. The resistivity decreased to about 5.55×10^{-4} Ω cm after annealing at 250°C for 2 h. All these results confirm the potential of annealed molybdenum-doped In_2O_3 thin film for use as a transparent conductive oxide in optoelectronic devices, especially as a transparent electrode or an optical window for solar cell devices.

REFERENCES

1. L.N. Lau, N.B. Ibrahim, and H. Baqiah, *Appl. Surf. Sci.* 345, 355 (2015).
2. M.A. Majeed Khan, W. Khan, M. Ahamed, and M. Alhoshan, *Mater. Lett.* 79, 119 (2012).
3. Z. Yuan, X. Zhu, X. Wang, X. Cai, B. Zhang, D. Qiu, and H. Wu, *Thin Solid Films* 519, 3254 (2011).
4. Y.H. Shin, S.B. Kang, S. Lee, J.J. Kim, and H.K. Kim, *Org. Electron.* 14, 926 (2013).
5. G. Korotcenkov, A. Cerneavschi, V. Brinzari, A. Vasiliev, M. Ivanov, A. Cornet, J. Morante, A. Cabot, and J. Arbiol, *Sens. Actuators B* 99, 297 (2004).
6. P. Prathap, N. Revathi, K.T. Ramakrishna Reddy, and R.W. Miles, *Thin Solid Films* 518, 1271 (2009).
7. S. Louidi, F.Z. Bentayeb, W. Tebib, J.J. Suñol, A.M. Mercier, and J.M. Grenèche, *J. Non-Cryst. Solids.* 356, 1052 (2010).
8. R. Swanepoel, *Phys. E: Sci. Instrum.* 16, 1214 (1983).
9. M. Ajili, M. Castagné, and N. Kamoun Turki, *Superlattices Microstruct.* 53, 213 (2013).
10. S. Kaleemulla, N. Madhusudhana Rao, M. Girish Joshi, A. Sivasankar Reddy, S. Uthanna, and P. Sreedhara Reddy, *J. Alloys Compd.* 504, 351 (2010).
11. M.J. Buerger, *X-ray crystallography* (New York: Wiley, 1960), p. 23.
12. M. Jothibas, C. Manoharan, S. Ramalingam, S. Dhanapandian, and M. Bououdina, *Spectrochim. Acta A* 122, 171 (2014).
13. S. Parthiban, V. Gokulakrishnan, K. Ramamurthi, E. Elangovan, R. Martins, E. Fortunato, and R. Ganesan, *Sol. Energy Mater. Sol. Cells* 93, 92 (2009).
14. N.G. Pramod and S.N. Pandey, *Ceram. Int.* 41, 527 (2015).
15. J. Tauc and A. Menth, *J. Non-Cryst. Solids* 8, 569 (1972).
16. G. Cabello, L. Lillo, C. Caro, G.E. Buono-Core, B. Chornik, and M.A. Soto, *J. Non-Cryst. Solids* 354, 3919 (2008).
17. S. Parthiban, E. Elangovan, K. Ramamurthi, R. Martins, and E. Fortunato, *Sol. Energy Mater. Sol. Cells* 94, 406 (2010).
18. M. Dhanasankar, K.K. Purushothaman, and G. Muralidharan, *Solid State Sci.* 12, 246 (2010).
19. P. Prathap, Y.P.V. Subbaiah, M. Devika, and K.T. Ramakrishna Reddy, *Mater. Chem. Phys.* 100, 375 (2006).
20. J.C. Manifacier, J. Gasiot, and J.P. Fillard, *J. Phys. E: Sci. Instrum.* 9, 1002 (1976).
21. W.L. Bragg and A.B. Pippard, *Acta Crystallogr.* 6, 865 (1953).
22. M. Harris, H.A. Macleod, and S. Ogura, *Thin Solid Films* 57, 173 (1979).
23. V. Senthilkumar, P. Vickraman, M. Jayachandran, and C. Sanjeeviraj, *Vacuum* 84, 864 (2010).
24. W.W. Mobzen, *J. Vac. Sci. Technol.* 12, 99 (1975).
25. S.H. Wemple and M. DiDomenico, *Phys. Rev. B.* 3, 1338 (1971).
26. N. Beji, M. Souli, M. Ajili, S. Azzaza, S. Alleg, and N. Kamoun Turki, *Superlattices Microstruct.* 81, 114 (2015).
27. N. Beji, M. Souli, S. Azzaza, S. Alleg, and N. Kamoun Turki, *J. Mater. Sci. Mater. Electron.* 27, 4849 (2016).
28. A. El Hichou, M. Addou, M. Mansori, and J. Ebothe, *Sol. Energy Mater. Sol. Cells* 93, 609 (2009).
29. E. Benamar, M. Rami, C. Messaoudi, D. Sayah, and A. Ennaoui, *Sol. Energy Mater. Sol. Cells* 56, 125 (1999).
30. B.L. Zhu, X.Z. Zhao, F.H. Su, G.H. Li, X.G. Wu, J. Wu, and R. Wu, *Vacuum* 84, 1280 (2010).
31. D.K. Kim and H.B. Kim, *Curr. Appl. Phys.* 13, 2001 (2013).
32. S. Cho, *Microelectron. Eng.* 89, 84 (2012).
33. C. Manoharan, S. Dhanapandian, A. Arunachalam, and M. Bououdina, *J. Alloys Compd.* 685, 395 (2016).
34. A. Rahal, A. Benhaoua, M. Jlassi, and B. Benhaoua, *Superlattices Microstruct.* 86, 403 (2015).